ELSEVIER

Journal of Nuclear Materials 265 (1999) 69–77

journal of nuclear materials

Dissolution of ZrO_2 in molten Zircaloy-4

P.J. Hayward *, I.M. George

Atomic Energy of Canada Limited, Whiteshell Laboratories, Pinawa, Manitoba, Canada R0E 1L0

Received 29 April 1998; accepted 31 August 1998

Abstract

Isothermal heating experiments within the temperature range 2000–2300°C have been used to study the dissolution of yttria-stabilized zirconia crucibles in molten Zircaloy-4, simulating the dissolution of steam-oxidized cladding in underlying molten alloy during a severe fuel-damage accident. Rapid crucible dissolution occurred during the first ~100 s of the 2100–2300°C tests, whereas, at 2000°C, the Zircaloy charge failed to melt. In all cases, however, O diffusion across the crucible/alloy interface formed a solid ZrO_{2-x} layer that grew with time and prevented further crucible dissolution. Subsequent changes to the alloy composition were produced by O-diffusion through this layer. These results differ from those of previous work, and suggest that the ZrO_2–dissolution correlation currently used in several reactor accident codes needs to be corrected. The use of stabilized zirconia crucibles to simulate steam-oxidized cladding is discussed.

1. Introduction

During the high-temperature transient phase of a severe-fuel-damage (SFD) reactor accident, decay heat from the fuel can cause the residual water to boil, forming a steam atmosphere in the top portion of the reactor vessel or fuel channel. Subsequent steam oxidation of the Zircaloy-4 (Zry) cladding will form a surface skin of ZrO_2. The oxidation reaction is highly exothermic and can become self-sustaining beyond ~1250°C. The evolved heat, together with heat from fission-product decay, may then drive fuel rod temperatures above the melting point ($\geqslant$ 1760°C) of any underlying cladding that has not been converted to ZrO_2.

The molten alloy, held in contact with the fuel by the outer layer of ZrO_2, will begin to dissolve both fuel and ZrO_2 simultaneously until failure of the oxide layer occurs. At this time, the molten Zr–U–O material will relocate in a manner dictated by the core geometry, mobilizing any dissolved fission products and releasing volatile fission products into the primary cooling circuit. This sequence of events, which produces pools of molten material around undissolved fuel in the lower reactor regions, has been observed in out-reactor [1] and in-reactor [2] tests.

Hence, the dissolution rate of the ZrO_2 surface layer on steam-oxidized cladding is an important factor in determining: (i) the fuel/molten cladding contact time; (ii) the amount of molten cladding available for fuel dissolution and (iii) the molten cladding oxygen content. The O content of the molten cladding also influences fuel solubility, with the solubility being depressed at higher O contents [3]. For these reasons, dissolution rate and solubility data for ZrO_2 in molten Zry are required input parameters for several SFD codes, including ICARE2 and SCDAP/RELAP5.

There are two possible mechanisms for ZrO_2 dissolution in molten Zry. If the volume of molten Zry is sufficient to allow melt circulation, dissolution may occur by natural-convection mass transfer. Ignoring the minor alloying elements (Sn, Fe, Cr) in Zry, the reaction may be represented by the equation

$$ZrO_2 + Zr_{(l)} \overset{\text{convective mass-transfer}}{\rightarrow} Zr(O)_{(l)}. \quad (1)$$

The influence of gravity in driving convection will be minimal, however, because the density difference between the solvent (molten Zry) and the reaction product (Zr(O)) is rather small. In this respect, therefore, the

* Corresponding author. Tel.: +1-204 753 8338; fax: +1-204 753-2455 e-mail: haywardp@mb.sympatico.ca.

0022-3115/99/$ – see front matter
PII: S0022-3115(98)00512-1

reaction differs from the case of UO_2 dissolution in molten Zry.

The second dissolution mechanism involves oxygen diffusion from the ZrO_2 layer to the underlying alloy and can occur both below and above the Zry melting temperature, according to the generalized equation

$$ZrO_2 + Zr \overset{\text{oxygen diffusion}}{\rightarrow} ZrO_{2-x} + Zr(O). \quad (2)$$

Depending on time, temperature and the relative amounts of oxide and alloy, the end product(s) of reaction (2) may be solid (α-) or liquid Zr(O), ZrO_{2-x} or co-existing [ZrO_{2-x} + Zr(O)]. Thinning or breaching of the oxide layer may also occur if there is sufficient alloy available to reduce the oxide to a composition outside the ZrO_{2-x} stability field.

The equilibrium solubility of ZrO_2 in liquid Zr can be deduced from the Zr–O phase diagram [4,5]. The O/Zr atomic ratio along the phase boundary representing the terminal solubility of O in liquid Zr is given by:

$$O/Zr = -99.445 + 0.1332T - 5.92 \times 10^{-5}T^2 + 8.816 \times 10^{-9}T^3 \quad (3)$$

with T in the range 2065–2710°C. Over a similar temperature range, the O/Zr ratio along the lower ZrO_{2-x} phase boundary is given by

$$O/Zr = 12.56 - 9.76 \times 10^{-3}T + 2.165 \times 10^{-6}T^2. \quad (4)$$

In some reactor accident scenarios, however, the predicted heating rates are very high (several hundred °C/s), with relatively short residence times (a few seconds) for the fuel elements at temperatures above the cladding melting point. Under these conditions, it is unlikely that chemical equilibrium between the ZrO_2 layer and underlying liquid metal would be achieved. Hence, the degree of oxide-layer thinning from ZrO_2 dissolution must be predicted from kinetic data rather than from equilibrium solubilities.

The only published dissolution data for ZrO_2 in molten Zry are those of Hofmann et al. [6], obtained from 2000°C to 2400°C isothermal heating experiments with molten Zry charges in CaO-stabilized zirconia crucibles. The use of stabilized (cubic, γ) zirconia was required to avoid the monoclinic/tetragonal (α/β) transition that occurs at ~1205°C in unstabilized zirconia: this transition produces a large (~9%) volume change in unstabilized zirconia ceramics and causes them to shatter during heating or cooling.

The melt regions in the cooled specimens from these experiments contained uniformly distributed ZrO_{2-x} and α-Zr(O) regions, indicating good convective stirring at the test temperature. The melts were analyzed indirectly by comparing the melt microstructures and phase contents with those of previously melted (equilibrated) ZrO_2/Zr standards. The amount of dissolved ZrO_2 in each crucible melt was then determined by correlating the measured area fraction of ZrO_{2-x} in the cooled melt with those in the standards. It was concluded that, after an initial brief period of very rapid ZrO_2 dissolution, the dissolution rate followed a parabolic law of the form

$$(W - C)^2 = kt, \quad (5)$$

where W is the ZrO_2 content of the melt (wt%), k is the parabolic rate constant and t is time. C, a constant representing the amount dissolved during the initial period of very rapid dissolution, was measured as 23.3 wt%.

One criticism of this analysis method is that the oxygen contents of the premelted standards were fixed by the initial ZrO_2/Zr quantities used, whereas, in the crucible experiments, further melt oxygenation could occur by O-diffusion from undissolved crucible material. Hence, when used to analyze the results of a crucible experiment, this method would give a value for the amount of dissolved ZrO_2 that was too high.

To overcome this problem, we have employed a more direct chemical analysis method to analyse melts from 2000°C to 2300°C tests in which Zry charges were isothermally heated for known times in yttria-stabilized ZrO_2 crucibles. These crucibles also contained ~1.4 wt% HfO_2 as a natural impurity. The ICP spectrometry analyses of the Hf content in each melt have been used to calculate the extent of crucible dissolution. The method relies on the assumption that Hf dissolves congruently with Zr, based on their similar chemical properties and almost identical ionic radii (0.144 and 0.145 nm, respectively, for Hf^{4+} and Zr^{4+}).

2. Experimental

2.1. Materials

Pressed 15-g compacts of yttria-stabilized zirconia powder [1] were fired in air at 1500°C for 1 h to produce sintered right cylinders of 13.85-mm diameter, 17-mm height, with no open porosity. The cylinders were then cored to produce a series of crucibles with 6.5-mm diameter, 14-mm deep cavities. Zry samples were machined from bar stock to fit the cavities, using a crucible/Zry mass ratio of 5.75 to completely fill the cavity after the Zry charge had melted. The Hf content of this material (manufacturer's ingot analysis) was 56 ± 5 ppm.

[1] American Vermiculite Corporation, Code H5Y-4.5SD. 7.9 wt% yttria.

2.2. Test procedure

The isothermal heating tests were performed under an ultra-high-purity (UHP) argon atmosphere in a programmable tungsten resistance furnace. In each test, the crucible/charge specimen was contained in an outer thin-walled thoria crucible to catch any spilled melt.

The furnace was initially evacuated and back-filled with UHP argon, then heated to ~1550°C and held at this temperature for about two minutes to allow temperature equilibration. A dual-wavelength pyrometer, focussed on the Zry charge through a fused quartz window in the furnace roof, was used to measure specimen temperatures at 1 s intervals, using a computer-based data-acquisition system. The accuracy of the temperature measurements is estimated to be ±16°C, based on prior calibration by the pyrometer manufacturers.

The specimen was then heated to the test temperature at the maximum rate achievable. The approach to temperature in each test was asymptotic, with the initial heating rate of ~11°C/s falling progressively to give a typical mean rate of ~7°C/s. At the end of each test, the specimen was cooled rapidly (~9°C/s) to 1500°C by turning off the furnace power. Below 1500°C, the furnace power was turned on again and then slowly reduced to allow the specimen to cool to room temperature over a period of ~1 h.

The target times were 1, 10, 25 or 60 min at 2000 and 2100°C, and 1, 10, 20 or 30 min at 2200 and 2300°C. The tests at 2100, 2200 and 2300°C were performed in duplicate to confirm that the results were reproducible. The time/temperature parameters for both series of tests are included in Table 1. Because of the time taken for the molten Zry to reach the isotherm temperature, it was impossible to accurately define the start of each isothermal test and, thus, the test duration. For this reason, we have arbitrarily taken the time of melting of the Zry charge, (shown on each time/temperature trace as a discontinuity caused by a thermal arrest and/or an emissivity change) as the start of the isothermal heating period. We emphasize, however, that this is merely one of several ways to define the reaction time.

The time/temperature parameters for both series of tests are included in Table 1. The 'Total Time Molten' column refers to the elapsed time between melting and turning off the furnace power, while the 'Main Part of Isotherm' column indicates the degree of temperature control achieved during the isothermal heating period.

2.3. Specimen analysis

Each post-test specimen was sectioned along the cylinder-axis plane, with one half being used for optical microscopy and SEM/EDX examinations and the other half for ICP emission spectrographic analysis. No ICP analyses were performed on the 2000°C specimens, however, because optical/SEM examinations showed that no crucible-wall dissolution had occurred, even though the Zry charge had melted.

Table 1
Zirconia–Zircaloy dissolution test parameters

Target (°C)	Total Time Molten (s)	Isothermal Temp (°C) and Time
2000	146	1995 ± 5, 83 s
2000	553	2006 ± 7, 542 s
2000	1506	2002 ± 5, 1441 s
2000	3615	2002 ± 7, 3528 s
2100	116	2100 ± 6, 41 s
2100	175	2103 ± 3, 44 s
2100	601	2100 ± 6, 497 s
2100	653	2103 ± 3, 464 s
2100	1490	2101 ± 4, 1384 s
2100	1500	2098 ± 9, 1441 s
2100	1523	2102 ± 3, 1377 s
2100	3418	2102 ± 7, 3627 s
2100	3585	2101 ± 3, 3522 s
2200	100	2201 ± 13, 46 s
2200	136	2205 ± 4, 64 s
2200	589	2202 ± 3, 489 s
2200	612	2207 ± 12, 515 s
2200	1191	2202 ± 4, 1076 s
2200	1197	2206 ± 8, 919 s
2200	1786	2205 ± 10, 1684 s
2200	1787	2200 ± 5, 1692 s
2200	1799	2203 ± 7, 1693 s
2300	187	2310 ± 14, 75 s
2300	248	2296 ± 7, 65 s
2300	599	2304 ± 7, 485 s
2300	617	2300 ± 6, 416 s
2300	1195	2300 ± 6, 1081 s
2300	1202	2302 ± 4, 1002 s
2300	1783	2301 ± 7, 1547 s
2300	1798	2300 ± 6, 1662 s

Samples of the melt regions from 2100°C to 2300°C test specimens were obtained as follows. A ~0.5-mm section of each specimen was cut parallel to the plane of original sectioning, and mounted on a supporting glass slide using a thermoplastic cement. The undissolved crucible material was removed from the section by careful cutting and grinding around the melt region. Any layered material at the crucible/melt interface was included in the analysis sample. Finally, the attached glass slide portion was removed by ultrasonic cleaning in methanol and acetone.

The samples were dissolved in HNO_3/HF and analysed by ICP for Zr, Hf, Y, Sn, Fe and Cr. The ceramic powder used for crucible fabrication was also analyzed for these elements, using a lithium tetraborate/lithium metaborate fusion method, followed by dissolving in 0.1% HNO_3. The precision (3σ) on the ICP analyses for

Zr and Hf was calculated from repeated measurements on one sample to be ±2.0%. In all cases, the O results from ICP analysis were obtained by difference.

The second half of each sectioned specimen was polished to a 1-μm finish and examined by reflected light microscopy and by SEM. Backscattered electron images were used for SEM examinations to allow the different phases to be distinguished by their atomic-number contrasts. The tone contrasts for the observed phases were in the following order: Zr or Zry darker than α-Zr(O); α-Zr(O) darker than ZrO_{2-x}. Qualitative EDX analyses were made to examine the distribution of minor elements (Sn, Y, Hf, Fe and Cr) in the individual phases; in most cases, however, their concentrations were below the EDX detection limits.

3. Results

3.1. ICP analytical results

The mean Hf/Zr ratio (wt%) in the unreacted crucible material, based on six ICP analyses, was $(21.03 \pm 0.46) \times 10^{-3}$. The mean Hf/Zr ratio (wt%) in the original Zry was $\sim 0.05 \times 10^{-3}$, and was therefore ignored in the subsequent calculations. The crucible Hf/Zr ratio was then combined with the ICP melt analyses for Hf to calculate the amount of dissolved crucible material in each melt. Fig. 1 shows $Zr_{crucible}/Zr_{total}$, the ratio of crucible-derived Zr in the melt to the total melt Zr content, plotted against the square root of time. It is particularly noteworthy that the ratios appear to undergo a slight *decrease* with increasing time at each temperature, i.e., the opposite trend to that found by Hofmann et al. [6]. This trend is discussed further in Section 4.1.

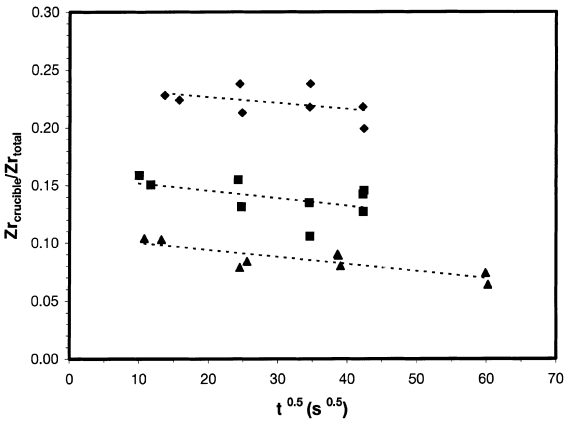

Fig. 1. Dissolved crucible fraction, based on melt Hf content, for specimens from tests at 2100°C (triangles), 2200°C (squares) and 2200°C (diamonds). Linear regression trend lines shown for data at each temperature.

3.2. SEM/EDX observations and analyses

Specimens representing differing times at each test temperature were used to produce low magnification (20x) backscattered electron micrographs, with the entire specimen being photographed in each case. The micrographs were then assembled by hand to form a composite image that accurately represented the whole sample. The tone contrast in these images was somewhat variable, however, and improved images were subsequently made by P. Hofmann and co-workers (FZK, Karlsruhe), using computer-enhanced reflected-light microscopy. Fig. 2(a)–(c) show a typical sequence of their images representing the 2100°C test series specimens after 1, 10 and 25 min, respectively. Fig. 2(d) shows their image of the 2000°C/10-min test specimen.

It was evident from the micrographs that no crucible dissolution had occurred in any of the 2000°C test specimens, whereas some dissolution of the sidewalls and bottom corners had occurred in the 2100–2300°C test specimens. In other respects, however, the micrographs demonstrated a similar reaction sequence. The notable features, which are illustrated diagramatically in Fig. 3, were as follows.

(i) The gradual development of a ZrO_{2-x} layer at the melt/crucible interface. The layer invariably exhibited a 'prior-cubic' microstructure containing coarse bands and additional fine lamellae of exsolved α-Zr(O), formed by eutectoid decomposition of ZrO_{2-x} during cooling through the γ/β and β/α transition temperatures at ~1500°C and ~1205°C, respectively [4,5]. These features are shown in Fig. 4(a) and (b).

(ii) Formation of a central melt region that, after cooling, contained a homogeneous microstructure of ZrO_{2-x} dendrites within an α-Zr(O) matrix, as shown in Fig. 5. The ZrO_{2-x} dendrites showed similar prior-cubic microstructural features and were present in greater amounts after longer reaction times. Occasional inclusions of $Zr_5Sn_3(O)$ and a Zr/Fe/Cr alloy were also observed in the melt matrix.

(iii) Progressive development of a convex melt meniscus.

In contrast to the ZrO_{2-x} layer at the crucible/melt interface, the residual crucibles did not exhibit prior-cubic microstructures, indicating that they had retained sufficient Y to stabilise the cubic structure. Nevertheless, the $(Zr,Y)O_{2-x}$ grain boundary regions contained traces of exsolved material, shown in Fig. 6. Although too small for EDX analysis, these regions alikely contained a metallic or oxygenated metal phase, producing the observed atomic number contrast.

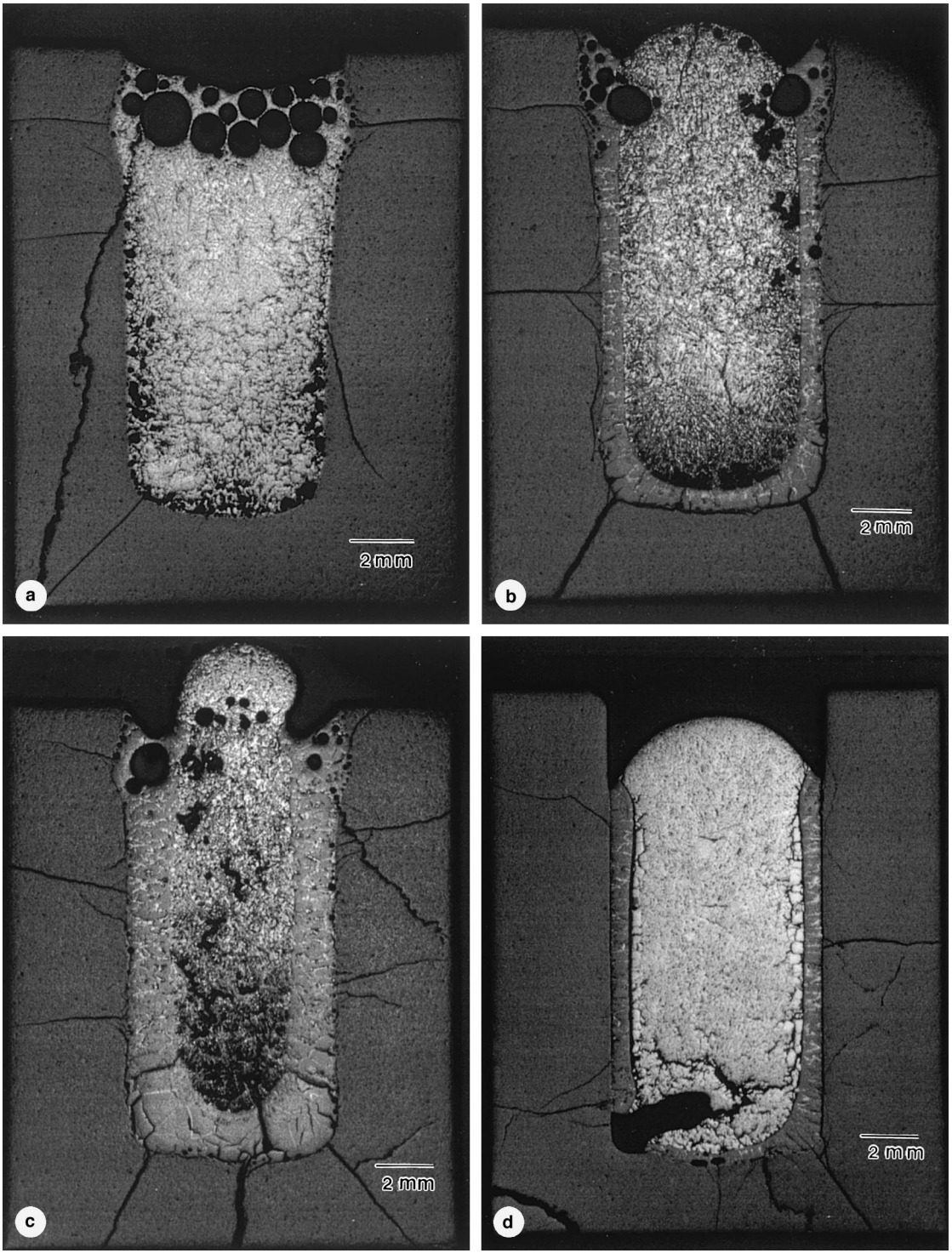

Fig. 2. Micrographs of sectioned crucibles from the following tests: (a) 2100°C/1-min; (b) 2100°C/10-min; (c) 2100°C/25-min and (d) 2000°C/10-min.

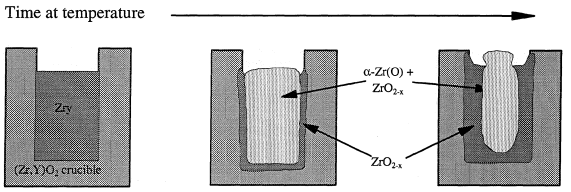

Fig. 3. Schematic diagram of sectioned crucibles, showing reaction progression at 2100–2300°C.

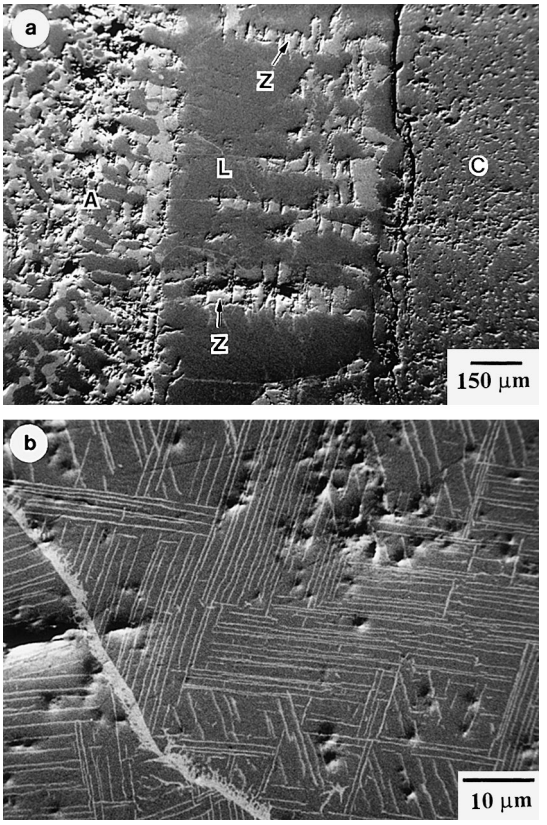

Fig. 4. Prior-cubic microstructure of ZrO_{2-x} layer (L) at interface between crucible (C) and alloy (A): (a) 2200°C/612-s specimen, showing coarse α-Zr(O) bands (Z) formed by the γ/β transition and (b) 2000°C/146-s specimen, showing fine lamellae of α-Zr(O) formed by the β/α transition.

4. Discussion

4.1. Influence of oxygen diffusivity on ZrO_2 dissolution

There is an obvious discrepancy between the trends of our ICP results and the data of Hofmann et al. [6]. Furthermore, we found no evidence for ZrO_2 dissolution in our 2000°C tests, although the presence of cooling voids in the bottom corners of each Zry charge indicated that the Zry had been molten for at least part of the test.

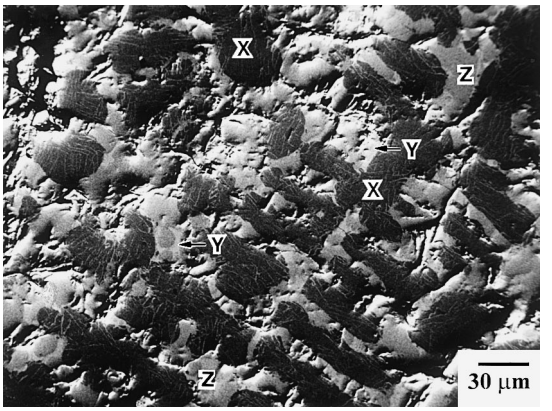

Fig. 5. Central melt region in a 2300°C/1195-s test specimen, showing prior-cubic ZrO_{2-x} (X), $Zr_5Sn_3(O)$ inclusions (Y) and the α-Zr(O) matrix (Z).

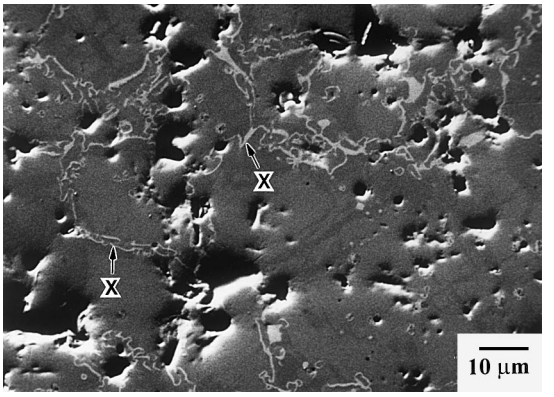

Fig. 6. Residual crucible microstructure in a 2000°C/1506-s test specimen showing exsolved material (X) at the $(Zr,Y)O_{2-x}$ grain boundaries.

Nevertheless, the microstructures of our 2000–2300°C test specimens are remarkably similar to those of the 2100°C melts shown in Ref. [6].

The lack of dissolution in our 2000°C specimens may be explained as follows. Dienst et al. [7] have shown that a finite time is required for molten Zry to become sufficiently O-enriched by diffusion to wet UO_2. It is reasonable to assume that similar O-enrichment must occur before molten Zry will wet a ZrO_2 crucible. Hence, we attribute the lack of dissolution at 2000°C to non-wetting of the crucible surfaces during the time taken for the liquid Zry at the crucible/melt interface to become sufficiently oxygenated for the melting temperature to exceed 2000°C. Thus, after a very short time interval at 2000°C, the crucible is protected from contact with liquid Zry in the central melt region by a boundary layer of solid Zr(O), and no further dissolution can occur.

Oxygen diffusion will continue through this layer, however, until the crucible composition reaches the lower ZrO_{2-x} phase boundary. The oxygenated melt solidifies at ~2065°C [4,5] during post-test cooling to form α-Zr(O) and γ-ZrO_{2-x}. On further cooling, the γ-ZrO_{2-x} undergoes transitions to β-ZrO_{2-x} at ~1500°C and to α-ZrO_{2-x} at ~1205°C, with exsolution of α-Zr(O) during each transition.

The α-Zr(O) and ZrO_{2-x} phases in the central melt regions of the 2100–2300°C test specimens are produced during post-test cooling by a similar sequence of reactions. In these tests, however, O-enrichment of the melt occurred by the combined effects of crucible dissolution and O diffusion.

The progressive growth of a ZrO_{2-x} layer at the crucible/melt interfaces in all of our test specimens is also evident in the optical micrographs of Ref. [6]. Berdyshev and Veshchunov [8,9] have proposed a dissolution model that accounts for growth of this layer in both sets of results. They note that the Ref. [6] micrographs show dissolution of the crucible sidewalls for the initial ~100 s of reaction (referred to as *erosion*). After this time, the solid/liquid boundary movement changes direction and produces a layer of ZrO_{2-x} at the interface (referred to as *corrosion*).

The direction and velocity of the interface movement is postulated to depend on flux-matching of oxygen in the convectively stirred melt and in the solid. During the erosion stage, the O-flux in the melt is greater than in the solid, so that dissolution prevails. As the concentration gradient across the liquid boundary layer adjacent to the solid decreases, however, the convective flux falls below the O flux from diffusion in the solid, causing the erosion stage to cease. Thereafter, the direction of interface movement is reversed and the corrosion stage commences.

Adapting this hypothesis to our 2100–2300°C test results, the following sequence of events is postulated.

(i) After a short time required for wetting of the crucible by the molten Zry, rapid convection-enhanced dissolution of the crucible walls commences, causing the melt to become enriched in two O atoms for every Zr atom that is dissolved. Simultaneous O enrichment of the melt from chemical diffusion also occurs. These factors produce a progressive reduction in the O concentration gradient across the crucible/melt interface, and, hence, in the thermodynamic driving force for dissolution.

(ii) The dissolution (erosion) process is terminated when the oxygen flux to the melt from diffusion exceeds the O-flux from dissolution. At this time, a layer of ZrO_{2-x} starts to form at the crucible/melt interface. This layer protects the underlying crucible from the melt, so that there is no subsequent increase in the Hf content of the melt.

(iii) Although the crucible wall is now protected by a growing layer of ZrO_{2-x}, there is still an oxygen concentration gradient across the layer/melt interface. Thus, the melt continues to become enriched in O, thereby increasing the volume fraction of ZrO_{2-x} dendrites formed in the final cooled melt.

Hence, according to this interpretation, the $Zr_{crucible}/Zr_{total}$ ratios should reach a maximum value at the end of the erosion stage and remain constant thereafter. In our results, however, the $Zr_{crucible}/Zr_{total}$ ratios appeared to *decrease* slightly with time (see Fig. 1). The decrease cannot be attributed to unequal Hf partitioning between the ZrO_{2-x} layer and the melt, either at temperature or during cooling, because the ICP samples included both the layer and the solidified melt, i.e., all material except the residual crucible. Indeed, it is hard to imagine a reaction mechanism that would produce a lower melt Hf content (and, thus, a lower $Zr_{crucible}/Zr_{total}$ ratio) at longer times. We conclude, therefore, that the slight decrease in $Zr_{crucible}/Zr_{total}$ ratio with time is probably an artifact produced by a small systematic error in the temperature and/or ICP measurements.

Fig. 7 shows the rate of increase in the mean ZrO_{2-x} layer thicknesses at mid-height in the 2000–2300°C specimens, based on measurements performed by J. Stuckert at FZK. Each mean value was derived from three measurements on digital images of selected specimens, with the measurements being made at locations between 1/3 and 2/3 of the cavity depth, i.e., covering the central 1/3 of the melt region.

The 2000°C data lie on a straight line with an intercept at 114 s. Thus, after an initial delay of 114 s (the crucible-wetting time), the ZrO_{2-x} layer thickness increased at a rate proportional to $t^{0.5}$, indicating diffusion-controlled growth. A value of $\sim 1.3 \times 10^{-9}$ m^2 s^{-1}

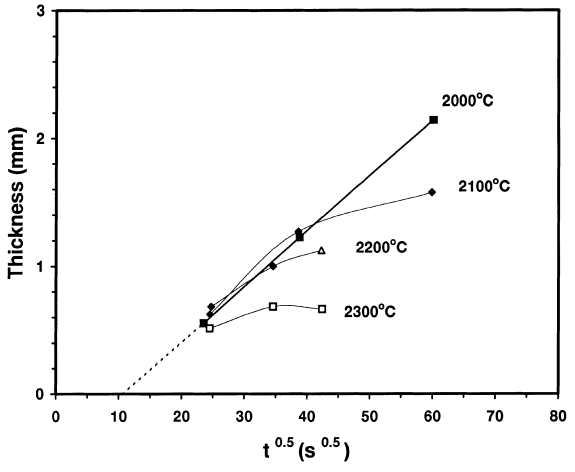

Fig. 7. Variation with time of the mean ZrO_{2-x} layer thickness at the crucible/melt interface.

for the chemical diffusion coefficient of oxygen ($\tilde{D}_O$) in unstabilized ZrO_{2-x} at 2000°C was calculated from the line slope. This value is in reasonable agreement with that of 5×10^{-9} m^2 s^{-1} obtained by extrapolating the 1050–1650°C diffusion data of Hofmann et al. [10] to 2000°C. Values for $\tilde{D}_O$ could not be calculated from the 2100–2300°C layer-thickness data, however, because each ZrO_{2-x} layer was formed by the combined effects of erosion and corrosion, i.e., was not produced solely by O diffusion.

In summary, the Berdyshev/Veshchunov hypothesis appears to resolve the major differences between our results and those of Hofmann et al. [6]. The analysis method used by these authors, i.e., comparison of the ceramic-phase content of their melts with those of standard mixtures, would naturally lead to the conclusion that crucible dissolution was continuing to occur with time, whereas our ICP melt analyses show that this is not the case.

4.2. Use of stabilized zirconia to simulate steam-oxidized cladding

Substitution of lower-valency cations (Y^{3+}, Ca^{2+}, Mg^{2+}, etc.) in ZrO_2 to stabilize the fluorite (cubic) structure creates a corresponding concentration of oxygen vacancies. In the case of yttria-stabilized zirconia, the Y_2O_3 concentration required for room-temperature stabilization is $\geqslant 5$ wt%. At higher temperatures, the degree of permissible Y_2O_3 substitution in fluorite-structured $(Zr,Y)O_{2-x}$ increases to a maximum of ~50 mol% Y_2O_3, when up to ~16% of the O sites may be vacant [11].

Unstabilized ZrO_2 may also exhibit substantial hypostoichiometry at high temperatures, with up to ~20% of vacant oxygen sites at ~2300°C [4,5]. Unlike the case with stabilized zirconia, however, the hypostoichiometry does not persist on cooling through the γ/β and β/α transitions, so that exsolution of α-Zr(O) occurs at each transition temperature. This is why a prior-cubic microstructure occurred in the ZrO_2 layers and melt-region dendrites in the test specimens, but not in the residual crucibles.

While there have been no *direct* measurements for $\tilde{D}_O$ in stabilized zirconia materials at $\geqslant 2000$°C, there have been numerous measurements of their high temperature ($\leqslant 1800$°C) electrical conductivity (σ), which is related to the oxygen self-diffusion coefficient (D) by the Nernst–Einstein equation:

$$\sigma = \frac{n(Ze)^2 D}{fkT}, \tag{6}$$

where Ze is the charge on the mobile ions, n is their concentration, f is a correlation factor (usually close to 1), k is the Boltzmann constant and T the absolute temperature. Comparison of the measured conductivities of Ca-stabilized zirconia with the D values obtained from O^{18} tracer-diffusion measurements within the temperature range 700–1100°C [12] shows that the charge is carried entirely by oxygen ions migrating across vacancies. Thus, there is a direct relationship between conductivity and D, and both increase proportionally with a rise in the O-vacancy concentration [13,14].

It seems reasonable to assume that chemical diffusion of O (i.e., under an O concentration gradient) in cubic (stabilized or high-temperature unstabilized) ZrO_{2-x} will also occur by a similar mechanism. Thus, an increase in the O-vacancy concentration will give a corresponding increase in $\tilde{D}_O$.

During an SFD accident, steam oxidation of the cladding will produce an oxide skin in which the oxygen vacancy concentration varies from zero at the outer surface (i.e., in contact with steam) to a value at the inner surface (i.e., the interface with the underlying alloy) that is determined by the ZrO_{2-x}/α-Zr(O) phase-boundary composition at the interface temperature. At temperatures below the melting point of α-Zr(O), this concentration gradient is produced entirely by O-diffusion.

In contrast, stabilized zirconia contains a high initial concentration of uniformly distributed oxygen vacancies. When heated in contact with solid or liquid Zircaloy, stabilized zirconia will develop an oxygen-vacancy concentration gradient as a result of O-diffusion, superimposed on the inital vacancy concentration. It follows, therefore, that the O-vacancy concentration gradient in stabilized zirconia during reaction with Zry will differ from that in steam oxidized cladding, so that the $\tilde{D}_O$ values in each material will also differ. For this reason, we conclude that crucible dissolution tests with stabilized zirconia, such as our work and that of Hofmann et al. [6], may not be a reliable method of predicting the dissolution rates of steam-oxidized cladding under reactor accident conditions.

5. Conclusions

The dissolution of steam-oxidized cladding surfaces in underlying molten Zry during the high-temperature transient phase of a reactor accident is strongly influenced by the mobility of oxygen in the surface oxide layer. Analyses of melts from isothermal heating experiments with yttria-stabilized zirconia crucibles indicate that rapid dissolution in molten Zry occurs at 2100–2300°C during the first ~100 s. After this time interval, a layer of ZrO_{2-x} is formed at the crucible/melt interface when the O flux produced by diffusion from the oxide to the molten alloy exceeds the O flux from oxide dissolution. This layer grows with time at a rate determined by

the O chemical diffusion coefficient within the layer and protects the crucible from further dissolution.

The results of these experiments confirm the visual observations of Hofmann et al. [6] from similar experiments using Ca-stabilized zirconia crucibles. Their different interpretation was based on an indirect analysis method, which did not account for O diffusion effects. Our new data suggests that ZrO_2 dissolution models based on the Hofmann et al. results, such as those used in the ICARE2 and SCDAP/RELAP5 codes, need to be corrected.

Diffusion of oxygen in fluorite-structured ZrO_2 almost certainly occurs by migration across O vacancies. Stabilized ZrO_2 contains a high initial concentration of uniformly distributed O-vacancies, whereas steam oxidized cladding will contain a O-vacancy concentration gradient that, under conditions of unlimited steam supply, is fixed by the ZrO_{2-x} phase boundary. Thus, O diffusivities in the two materials may differ, so that the results of dissolution tests with stabilized zirconia crucibles must be used with caution in modelling the dissolution of steam-oxidized cladding in molten Zry.

Acknowledgements

We thank P. Hofmann, D.R. Olander, M.S. Veshchunov, B. Adroguer, R. Gonzales, D.G. Evans, P. Taylor, D.J. Wren and H.M. Hayward for their valuable manuscript reviews and/or comments. We are particularly grateful to A. Miassoedev for the photographs used in Fig. 2, to J. Stuckert for the data used in Fig. 7, and to P. Hofmann and M.S. Veshchunov for their ongoing interest in the work. We also thank K. Wazney for performing the ICP analyses. Financial support for this work was provided by the CANDU Owners Group, consisting of AECL, Ontario Hydro, Hydro-Quebec and NB Power.

References

[1] L. Sepold, Forschungszentrum Karlsruhe, Report No. FZKA-5570 (1995).
[2] P. von der Hardt (Ed), IPSN/JRC Report CPF177 (1996).
[3] P.J. Hayward, I.M. George, J. Nucl. Mater. 232 (1996) 1.
[4] J.P. Abriata, J. Garces, R. Versaci, Bull. Alloy Phase Diagrams 7 (1986) 116.
[5] W.-E. Wang, D.R. Olander, J. Am. Ceram. Soc. 76 (1993) 1242.
[6] P. Hofmann, Ch. Adelhelm, E. Garcia, M. Markiewicz, J. Burbach, G. Gaussmann, K. Kurz, H. Metzger, Report No. KfK-4200, September 1987, pp. 9–27.
[7] W. Dienst, P. Hofmann, D. Kerwin-Peck, Nucl. Technol. 65 (1983) 109.
[8] A.V. Berdyshev, M.S. Veshchunov, Unpublished report FZK, Karlsruhe, NSI-SARR-51-97, 1997.
[9] M.S. veshchunov, A.V. Berdyshev, J. Nucl. Mater. 252 (1998) 98.
[10] P. Hofmann, H. Uetsuka, E.A. Garcia, A. Denis, J. Nucl. Mater. 189 (1992) 46.
[11] R.S. Roth, J.R. Dennis, H.F. McMurdie (Eds.), Phase Diagrams for Ceramists, vol. VI, American Ceramic Society, Westerville, Ohio, 1987, pp. 182–184.
[12] W.D. Kingery, J. Pappis, M.E. Doty, D.C. Hill, J. Amer. Ceram. Soc. 42 (1959) 393.
[13] L.L. Hench, J.K. West, Principles of Electronic Ceramics, Wiley, New York, 1990, p. 156.
[14] W.D. Kingery, H.K. Bowen, D.R. Uhlmann, Introduction to Ceramics, 2nd ed., Wiley, New York, 1976, pp. 239–241.